Second and third order sub-harmonic wave responses of a floating wind turbine

Orszaghova, J.; Taylor, P. H.; Wolgamot, H.; Madsen, F. J.; Pegalajar-Jurado, A.; Bredmose, H.

Publication date:
2020

Document Version
Publisher's PDF, also known as Version of record

The 35th International Workshop on Water Waves and Floating Bodies, Seoul, Korea, 26-29 April 2020.

Second and third order sub-harmonic wave responses of a floating wind turbine

J. Orszaghova[1], P.H. Taylor[1], H. Wolgamot[1], F.J. Madsen[2], A. Pegalajar-Jurado[2], H. Bredmose[2]
[1] Faculty of Engineering and Mathematical Sciences, University of Western Australia, Australia.
jana.orszaghova@uwa.edu.au
[2] Department of Wind Energy, Technical University of Denmark, Kgs. Lyngby, Denmark.

INTRODUCTION

The expansion of offshore wind farms into deeper water requires floating concepts, as bottom-fixed monopile turbines become prohibitively expensive. In this work, a catenary moored floater system is investigated. Such systems typically have large natural periods in those modes where the hydrostatic stiffness is small (or zero), as the restoring force provided by the mooring is low. Since the hydrodynamic damping is weak, the systems are highly resonant. It is well known that low-frequency resonant motions of soft moored structures can be excited by second-order hydrodynamic loads. Here, we show that, for the floater considered, third-order difference interactions can also give rise to considerable resonant pitch motions.

EXPERIMENTS

A comprehensive laboratory campaign investigating responses of a model-scale floating wind turbine under wave and wind forcing was carried out in 2017 in the deep water basin at DHI, Hørsholm, Denmark. In this work, we focus on the hydrodynamics alone, analysing tests in the absence of wind. The tested turbine was a 1:60 scale model of the DTU 10MW reference wind turbine. The TetraSpar floater (yellow structure in Fig. 1), designed by Stiesdal Offshore Technologies, consists of a main column connected to three sets of tanks, as well as a triangular counterweight suspended from these. Attached to the tanks, three catenary mooring chains (in a symmetric arrangement, with one line pointing down-wave, and two lines pointing obliquely up-wave) were used to soft moor the floater. Here, we analyse the spar configuration where the tanks were completely submerged.

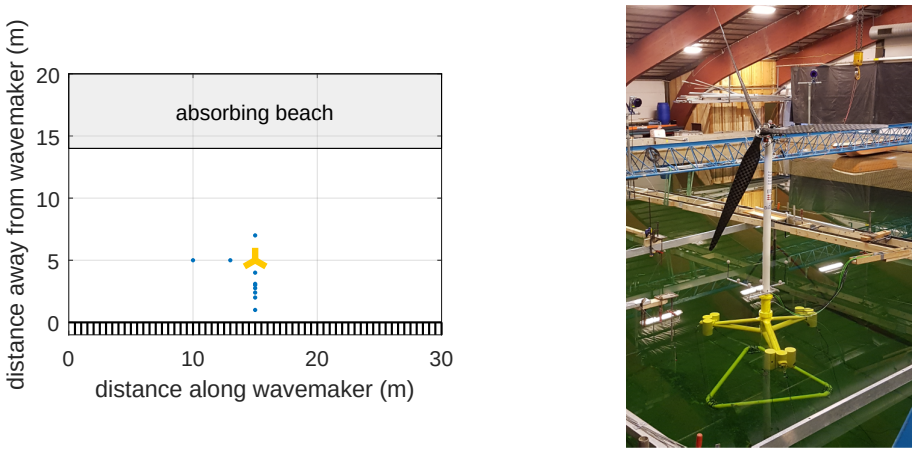

Fig. 1: Left: Diagram of the wave basin, with wave gauges (blue) and the model (yellow). Right: Photograph of the model wind turbine with the floater.

The wave basin is 30 m wide and 20 m long, with an articulated flap wavemaker (see Fig. 1). The water depth was 3 m. A number of wave gauges were used to measure the free surface elevation. A Qualisys optical motion tracking system was employed to measure the 6 degrees of freedom (DoF) motions of the floater. An extensive range of additional instrumentation was employed to measure tower and nacelle accelerations, mooring loads, as well as wind speed and rotor behaviour. Further details on the campaign are given in Borg et al. (2018). See also Bredmose et al. (2017) for details on the model turbine.

A number of different long-crested wave conditions were tested, including regular wave tests, long duration irregular wave tests as well as focused wave group tests. In order to facilitate separation of individual harmonics under the broad-banded wave conditions, phase-manipulated tests were carried out. In this work we analyse the floater dynamics in an extreme sea state with an underlying Pierson-Moskowitz spectral shape with significant wave height $H_s = 10.5$ m and peak period $T_p = 14.2$ s (corresponding to 0.175 m and 1.833 s in model scale). This random wave run was roughly 800 wave periods long.

DATA ANALYSIS AND RESULTS

The measured floater surge, heave and pitch motions exhibit notable responses at the natural frequencies, as well as in the range of the incident wave energy. Since, for the floater considered, the natural frequencies of all 6DoF lie below the typical incident wave frequencies, the motion at the natural frequencies must be driven non-linearly. The top plots in Fig. 2 show the pitch motion (θ) spectrum on the left and the linearised wave (η) spectrum on the right. The calculated pitch natural frequency (0.23 Hz), assuming linear hydrostatic and mooring restoring moments, is shown with the vertical green line.

Utilising two realisations, whereby the phase of every component has been shifted by 180° between the two runs (equivalent to inverting the linear paddle signal), even and odd order harmonics can be separated via addition and subtraction of the two signals (e.g. Fitzgerald et al. (2014)).

$$\begin{aligned}\frac{1}{2}\Big(X_0 - X_{180}\Big) &= A\beta_{11}\cos\phi + A^3(\beta_{33}\cos 3\phi + \beta_{31}\cos\phi) + O(A^5)\\ \frac{1}{2}\Big(X_0 + X_{180}\Big) &= A^2(\beta_{22}\cos 2\phi + \beta_{20}) + A^4(\beta_{44}\cos 4\phi + \beta_{42}\cos 2\phi + \beta_{40}) + O(A^6),\end{aligned}$$

where X_0 and X_{180} represent the two phase-shifted signals. The harmonic separation holds for broad-banded processes. However, here a narrow-banded representation has been used to simplify the notation, whereby A denotes the slowly-varying amplitude and $\phi = \omega t + p_0$ with ω and p_0 representing the carrier wave frequency and phase. The coefficients β_{ij} represent linear and higher order transfer functions. Focusing on the odd harmonics signal, the third order super-harmonic components β_{33} can be isolated by frequency filtering. However, the linear β_{11} and the third order sub-harmonic β_{31} components cannot be separated as their frequency ranges overlap. Usually, the third order terms (proportional to A^3) are much smaller and as such the subtraction timeseries largely represents the linearised signal.

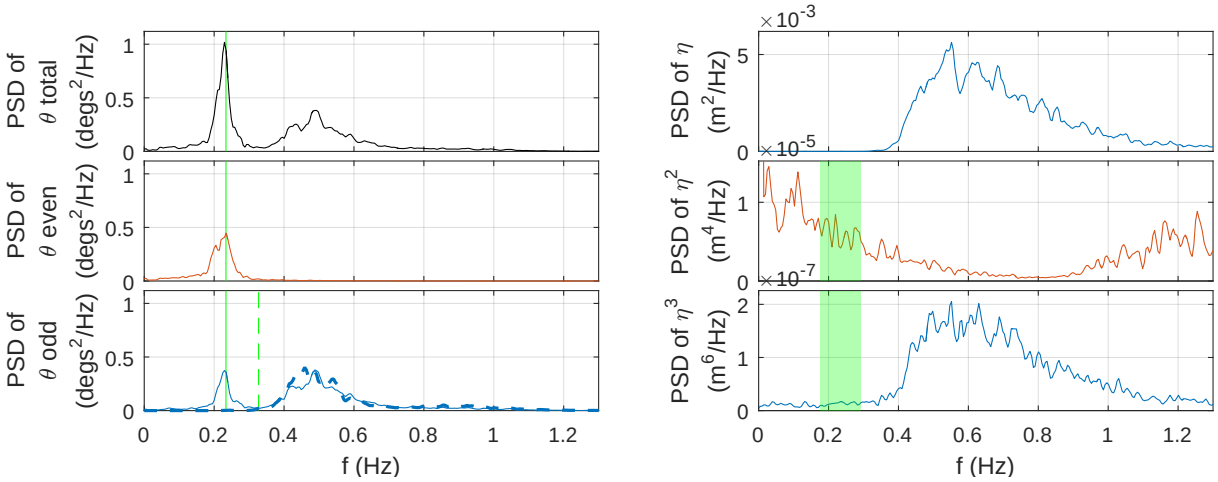

Fig. 2: Left: Variance density spectra of the floater pitch motion θ. The green vertical line denotes the calculated pitch natural frequency. The green dashed vertical line denotes the cut-off frequency used in the low-pass filter (LPF) applied to the odd pitch timeseries. The dashed blue curve represents the calculated linear pitch motion. Right: Variance density spectra of the linearised free surface η (raised to powers 1, 2 and 3). The green area denotes the frequency range of the band-pass filter (BPF) applied to the η^2 and η^3 timeseries.

The separation is applied to both the free surface and the motion signals. The left plots in Fig 2 show spectra of the total, as well as the even (red) and the odd (blue) pitch motion. We would expect

the response at the low natural frequency to appear in the even signal due to second order sub-harmonic wave-floater interactions. However, a comparably large response at the natural frequency also manifests in the odd signal. As mentioned above, there is virtually no linear excitation at the natural frequency. The fact that this motion is not driven linearly is confirmed by calculation of linear motion, which completely fails to reproduce the peak at the natural frequency (dashed blue curve in the bottom left plot). This calculation is done via a theoretical pitch response amplitude operator (based on the work of Pegalajar-Jurado et al. (2018)) applied to the linearised free surface η.

In order to identify the source of the odd pitch motion at the natural frequency, we use signal conditioning (similar to Zhao et al. (2018)). The linearised free surface raised to the n^{th} power, i.e. η^n, represents the n^{th} order bound waves, assuming unit transfer function/kernel values (see Walker et al. (2004)). It is thus a proxy for the n^{th} order forcing (which is generally due to contributions from both the local n^{th} order processes and the simple scattering of the n^{th} harmonic of the incident wave). Fig. 2 shows spectra of η^2 and η^3. The second-order sub-harmonic components can be seen on the left of the η^2 plot (below 0.4 Hz), and the super-harmonic components on the right (above 1 Hz). The third order sub-harmonic content in the η^3 plot can be seen overlapping with the linear frequencies, prohibiting separation, as mentioned above. Both the second and third order sub-harmonics span the pitch natural frequency. As we are interested in the pitch response around the natural frequency, we band-pass filter (BPF) η^n as shown in Fig. 2. The conditioning analysis involves selecting a number (here 30) of large events in the conditioning signal, as well as the corresponding sections of the conditioned signal. The remaining structure in the averaged signals is indicative of the coupling between the two processes, as the mean conditioned signal with no phase relationship to the mean conditioning signal would simply reduce to noise. Fig. 3 shows the even and odd pitch motion conditioned on second and third powers of η. Note that the odd pitch motion timeseries has been low-pass filtered (LPF) to remove the linearly excited motions. The conditioning signals are locally symmetric, as expected. The plots clearly suggest a coupling between η^2 and even pitch, and η^3 and low-pass filtered odd pitch, confirming that these are caused by quadratic and cubic interactions respectively.

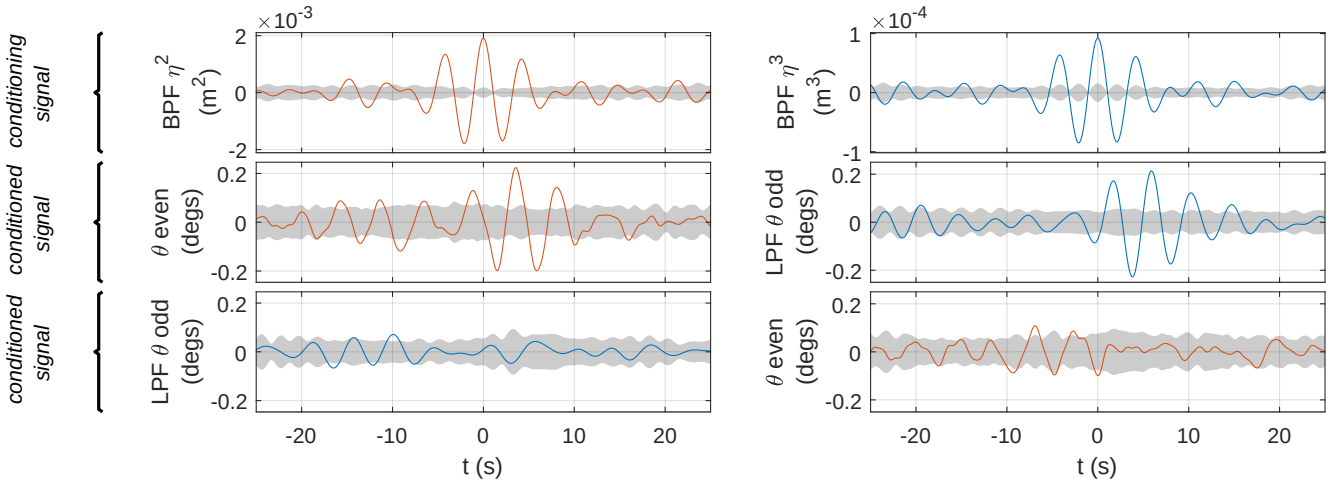

Fig. 3: Local average profiles of even and low-pass filtered odd pitch motion (second and third row) conditioned on extrema in the band-pass filtered η^2 and η^3 timeseries (first row). The grey shading represents 95% confidence intervals on the estimation of the mean signals.

The conditioned signal analysis can also be performed in reverse, whereby we condition on large even/odd pitch events. The equivalent plots to Fig. 3 are omitted for brevity. However, we utilise the resulting conditioned signals to highlight reciprocity between the two sets of coupled processes. For a linear system of two Gaussian processes (with a linear relationship between input and output), the averaged output signal conditioned on an extreme input event is identical to the scaled time-reversed/mirrored averaged input signal conditioned on an extreme output event. The derivation of this reciprocity relation is omitted here, but can be found in Zhao et al. (2018) for example. Each plot in Fig. 4 shows the

mean pitch time history associated with extrema in η^n (solid curve) and the mean η^n signal which gives the largest pitch response (dash-dotted curve). Note that the time axis has been reversed for the η^n timeseries. Each pair of curves shows a distinct similarity. Note that of course the quadratic and cubic interactions are pair- and triplet-wise. However, between a higher-order response and the corresponding higher-order forcing signal there is a linear relationship. In other words, the non-linear forcing operates through a linear transfer function, which we have confirmed with this reciprocity analysis.

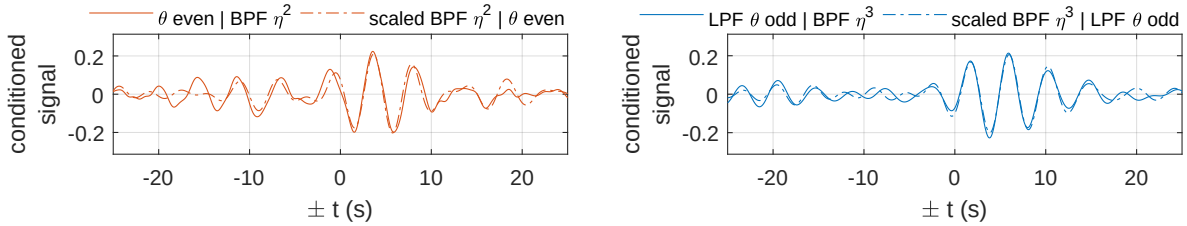

Fig. 4: Conditioned signals of even pitch motion and scaled η^2 (left) and low-pass filtered odd pitch motion and scaled η^3 (right). The time axis has been reversed for the η^n. In the label, the symbol | represents 'conditioned on'. The scaling factors applied to the conditioned η^2 and η^3 timeseries are 1.9×10^2 and 3.9×10^3 respectively.

CONCLUSIONS

The dynamic motion of a model-scale floating wind turbine is analysed to reveal non-linear resonant motions excited by cubic as well as quadratic hydrodynamic forcing terms. Identification of the third-order difference-frequency response has been possible due to harmonic separation using phase-manipulated realisations and conditioned signal analysis. The third order pitch motion is not negligible and in fact is of comparable magnitude to the second-order response. This could have implications for design, as currently third-order interactions are not considered.

At the workshop we hope to present further analysis for the other modes of motion, as well as for runs with combined wind and wave forcing.

ACKNOWLEDGEMENTS

This research was supported by Innovation Fund Denmark as part of the FloatStep project (grant no. 8055-00075A). HW and JO also acknowledge support from the UWA Research Priorities Fund. We wish to thank DTU and DHI staff (Bjarne Jensen and Jesper Fuchs) for their help in the experimental campaign. HW acknowledges financial support from Shell Australia and from the Lloyds Register Foundation.

REFERENCES

Borg, M., Bredmose, H., Stiesdal, H., Jensen, B., Mikkelsen, R., Mirzaei, M., Pegalajar-Jurado, A., Madsen, F., Nielsen, T., and Lomholt, A. Physical model testing of the TetraSpar floater in two configurations. In *15th Deep Sea Offshore Wind R&D Conference (EERA DeepWind)*, Trondheim, Norway, January 2018.

Bredmose, H., Lemmer, F., Borg, M., Pegalajar-Jurado, A., Mikkelsen, R., Stoklund Larsen, T., Fjelstrup, T., Yu, W., Lomholt, A., Boehm, L., and Armendariz, J. A. The triple spar campaign: Model tests of a 10MW floating wind turbine with waves, wind and pitch control. *Energy Procedia*, 137:58 – 76, 2017. doi: https://doi.org/10.1016/j.egypro.2017.10.334.

Fitzgerald, C., Taylor, P., Eatock Taylor, R., Grice, J., and Zang, J. Phase manipulation and the harmonic components of ringing forces on a surface-piercing column. *Proceedings of the Royal Society A-Mathematical Physical and Engineering Sciences*, 470, 2014. doi: 10.1098/rspa.2013.0847.

Pegalajar-Jurado, A., Borg, M., and Bredmose, H. An efficient frequency-domain model for quick load analysis of floating offshore wind turbines. *Wind Energy Science*, 3(2):693–712, 2018. ISSN 2366-7443. doi: 10.5194/wes-3-693-2018.

Walker, D., Taylor, P., and Eatock Taylor, R. The shape of large surface waves on the open sea and the Draupner New Year wave. *Applied Ocean Research*, 26(3), 2004. doi: 10.1016/j.apor.2005.02.001.

Zhao, W., Taylor, P., Wolgamot, H., and Eatock Taylor, R. Identifying linear and nonlinear coupling between fluid sloshing in tanks, roll of a barge and external free-surface waves. *Journal of Fluid Mechanics*, 844, 2018. doi: 10.1017/jfm.2018.186.